RESEARCH ARTICLE

Check for updates

β-Diketiminate-supported iridium photosensitizers with increased excited-state reducing power†

Jong-Hwa Shon, [ID] [a] Dooyoung Kim, [ID] [a] Thomas G. Gray [ID] [b] and Thomas S. Teets [ID] *[a]

A series of bis-cyclometalated iridium complexes were prepared which combine triazole or NHC-based cyclometalating ligands with substituted β-diketiminate (NacNac) ancillary ligands. The HOMO is localized on the NacNac ligand and its energy and associated redox potential are determined by the NacNac substitution pattern. The effect of the cyclometalating ligand, relative to the more common 2-phenylpyridine derivatives, is to destabilize the LUMO and increase the triplet excited-state energy (E_{T1}). These results are supported by DFT calculations, which show HOMOs and LUMOs that are respectively localized on the NacNac and cyclometalating ligands. With this new design, we observe more negative excited-state reduction potentials, $E(Ir^{IV}/*Ir^{III})$, with two members of the series standing out as the most potent visible-light iridium photoreductants ever reported. Stern–Volmer quenching experiments with ketone acceptors (benzophenone and acetophenone) show that the increased thermodynamic driving force for photoinduced electron-transfer correlates with faster rates relative to *fac*-Ir(ppy)$_3$ and previous generations of NacNac-supported iridium complexes. A small selection of photoredox transformations is shown, demonstrating that these new photoreductants are capable of activating challenging organohalide substrates, albeit with modest conversion.

Introduction

Transition metal-based photosensitizers are widely used in photocatalysis, harvesting light and participating in single-electron transfer (SET) or energy transfer (EnT) elementary steps, which initiate catalytic transformations in organic synthesis,[1] CO$_2$ reduction,[2] polymerization,[3] and solar fuels applications.[4,5] Of the many photosensitizer-based applications, organic synthesis *via* photoredox catalysis is a particularly fast-emerging area, with several pioneering research groups leading the way.[1,6–15] For several decades, the attractive homoleptic ruthenium or iridium-based photosensitizers, with their well-defined photophysical properties and catalytic stability, have been applied in many organic syntheses in combination with a cocatalyst or supporting additives.[6–8,16] That said, the development of strong visible-light photooxidants or photoreductants is in continued demand, since the organic substrates that can be activated are limited by the (excited-state) redox properties of the photosensitizer.

Of the large variety of available metal-based photosensitizers,[17] homoleptic Ir-based organometallic complexes, *fac*-Ir(ppy)$_3$ (ppy = 2-phenylpyridine) and its derivatives,[18] are known as some of the strongest photoreductants. Based on their strong reducing ability, several new synthetic methods have been reported using this photosensitizer with substrates that are challenging to reduce.[8,19–22] While *fac*-Ir(ppy)$_3$ maintains prominence in the organic synthesis field, heteroleptic iridium-based photosensitizers are emerging candidates for the next generation of photocatalysts with easily modifiable photophysical and electrochemical properties *via* ligand substitution. Bernhard and co-workers have developed a series of iridium-based photosensitizers of the [Ir(C^Y)$_2$(N^N)]$^+$ structure type (C^Y = 2-phenylpyridine and its derivatives, N^N = 2,2′-bipyridine and its derivatives).[23,24] These compounds are less photoreducing than *fac*-Ir(ppy)$_3$, but with judicious ligand choice can be strong photooxidants,[23] making them a versatile class of photosensitizers for catalytic applications.

Whereas Bernhard and others' efforts have improved the photooxidizing capability of iridium sensitizers, some of the more recent developments on metal-based photoreductants more potent than *fac*-Ir(ppy)$_3$ have involved other transition metals. Homoleptic tungsten-based photosensitizers in the

^{a}*University of Houston, Department of Chemistry, 3585 Cullen Blvd., Room 112, Houston, TX 77204-5003, USA. E-mail: tteets@uh.edu*
^{b}*Case Western Reserve University, Department of Chemistry, 10900 Euclid Ave., Cleveland, OH 44106, USA*

This journal is © the Partner Organisations 2021

Inorg. Chem. Front., 2021, **8**, 3253–3265 | **3253**

W(CNAr)$_6$ family, reported by Gray *et al.*,[25] have excited state reduction potentials as negative as −2.8 V (*vs.* Fc$^{+/0}$), 700 mV more negative than the reducing potential of *fac*-Ir(ppy)$_3$. Wenger *et al.* have reported molybdenum photosensitizers supported by chelating isocyanides, strong photoreductants with −2.6 V excited-state potentials.[26,27] There have been a few studies involving ligand modification of iridium-based photosensitizers to produce stronger photoreductants. These include Wenger *et al.*'s recent report of a water-soluble sulfonate-substituted homoleptic iridium photosensitizer, *fac*-Ir(sppy)$_3$, which generates solvated electrons *via* two-photon excitation.[19] In addition, a recent study from Connell *et al.* demonstrated that semi-reduction of the substituted 2,2′-bipyridine ancillary ligand in a cationic [Ir(C^Y)$_2$(N^N)]$^+$ sensitizer, which occurs under typical photoredox conditions, generates a charge-neutral complex which is as strong of a photoreductant as *fac*-Ir(ppy)$_3$ and capable of activating recalcitrant substrates.[28]

In our recent efforts, we have prepared a series of heteroleptic iridium photosensitizers supported by electron-rich β-diketiminate (NacNac) ancillary ligands. These compounds are stronger photoreductants than *fac*-Ir(ppy)$_3$ by ∼300–500 mV, resulting in improved photoinduced electron transfer rates.[29,30] Members of this series are also active in a wide range of photoredox transformations involving challenging substrates.[30,31] Our development of this new class of photosensitizer focused primarily on modifying the NacNac ancillary ligand, which controls the HOMO energy and results in large cathodic shifts of the first oxidation potential. Nevertheless, the destabilization of the HOMO energy level also leads to a drop in excited-state energy (E_{T1}), which attenuates the increase of the excited-state potential. These two effects largely cancel one another as the NacNac substituents are varied. As a result, the 13 variants we have prepared,[30] despite spanning a wide range of ground-state redox potentials, all have excited-state potentials falling in the narrow range of −2.4 to −2.6 V. To break through this "ceiling", in this work we made synthetic modifications to increase the excited-state energy (E_{T1}) as a means of accessing compounds that have even more negative excited-state reduction potentials. Recognizing that the HOMO energy and first oxidation potential are largely dictated by the NacNac ligand, our strategy employs triazole and NHC-based cyclometalating (C^Y) ligands, moving away from the 2-phenylpyridine family we mainly used in our previous work. These alternative C^Y ligands result in an increase in the LUMO and triplet-state energies, providing access to the most potent cyclometalated iridium photoreductants ever reported. The synthesis and structural, electrochemical, and photophysical characterization of six new Ir(C^Y)$_2$(NacNac) complexes are described, with DFT calculations providing insight into the frontier orbitals and redox processes. To demonstrate the efficacy of these improved photosensitizers, we have investigated photoinduced electron-transfer reactions to organic quenchers and screened photocatalytic hydrodehalogenation reactions with select organic halide substrates.

Results

Synthesis and structural characterization

In this work, we describe six new bis-cyclometalated iridium complexes of the general formula Ir(C^Y)$_2$(NacNac^R), where C^Y is the cyclometalating ligand and NacNac^R is a substituted β-diketiminate. Their structures are summarized in Fig. 1, along with the structures of four reference compounds that will be referred to throughout this work. Having previously paired these NacNac ligands primarily with 2-phenylpyridine (ppy) in a large number of Ir(ppy)$_2$(NacNac^R) complexes,[30,32] including **7–9** in Fig. 1, our goal in this work was to incorporate C^Y ligands that would engender higher excited-state energies. Previously developed blue-emitting iridium chromophores[33,34] provide insight into how to accomplish this goal, and we selected a 5-phenyl-1,2,4-triazole (ptz) and an *N*-phenyl benzimidazol-2-ylidine NHC (pmb) cyclometalating ligand to partner with the four NacNac ligands. The complexes are prepared *via* a general route involving reaction between [Ir(C^Y)$_2$(μ-Cl)]$_2$ dimers and the lithium or potassium salt of the deprotonated NacNac ligand. The compounds were all characterized by ^{1}H and ^{13}C{^{1}H} NMR, with the spectra shown in Fig. S1–S12 of the ESI.† The NMR spectra are consistent with the expected C_2 symmetry of the compounds and confirm that they were all isolated in pure form, free of diamagnetic impurities.
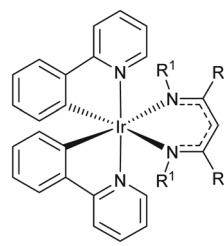

Compounds introduced here:
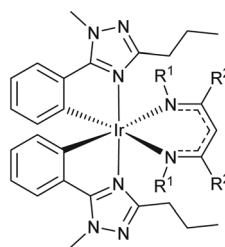
Ir(ptz)$_2$(NacNac^R)
1: NacNac^{NMe2} (R^1 = Ph, R^2 = NMe$_2$)
2: NacNac^{Cy} (R^1 = Cy, R^2 = Me)
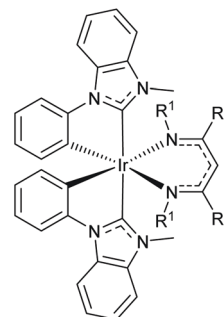
Ir(pmb)$_2$(NacNac^R)
3: NacNac^{OEt} (R^1 = Ph, R^2 = OEt)
4: NacNac^{Me} (R^1 = Ph, R^2 = Me)
5: NacNac^{NMe2} (R^1 = Ph, R^2 = NMe$_2$)
6: NacNac^{Cy} (R^1 = Cy, R^2 = Me)

Reference compounds:

Ir(ppy)$_2$(NacNac^R)
7: NacNac^{NMe2} (R^1 = Ph, R^2 = NMe$_2$)
8: NacNac^{Cy} (R^1 = Cy, R^2 = Me)
9: NacNac^{Me} (R^1 = Ph, R^2 = Me)
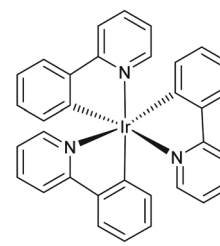
10: *fac*-Ir(ppy)$_3$

Fig. 1 Structures of compounds described in this paper.

3254 | *Inorg. Chem. Front.*, 2021, **8**, 3253–3265

This journal is © the Partner Organisations 2021

The molecular structures of all new complexes except **2** have been confirmed by single-crystal X-ray diffraction. The structures are shown in Fig. 2. In all cases, the triazole (complex **1**) or NHC (complexes **3**–**6**) L donors remain in a *trans* configuration, as is typically the case for bis-cyclometalated iridium complexes. In complexes **3**, **4**, and **6** the 1,5-diazapentadienyl core of the NacNac ligand exhibits a planar, π-delocalized structure, as we have observed for the vast majority of related compounds we have previously studied.[30,32,35–37] However, the NacNac^{NMe_2} ligand in complexes **1** and **5** adopts two different conformations. In pmb complex **5**, there is a buckling of the NacNac core that distorts it from planarity, which we have previously observed in a few other NacNac^{NMe_2} complexes.[30,32] In this conformation the NMe$_2$ groups are nearly coplanar with the three NacNac carbon atoms, allowing conjugation outside of the chelate ring. In contrast, the NacNac^{NMe_2} core in ptz complex **1** is akin to the rest of the complexes, forming a planar six-member chelate ring. We believe this difference arises from steric effects, with the propyl groups in the ptz ligands dangling over the NacNac plane and preventing the buckling distortion that often occurs in the solid-state structures of other NacNac^{NMe_2} complexes.

Ground-state redox properties

The ground-state first oxidation potentials, $E(Ir^{IV}/Ir^{III})$, were measured with cyclic voltammetry and they are listed in Table 1 with the voltammograms shown in Fig. S13 of the ESI.† The peak-to-peak separations (ΔE_p) for this redox wave span 63–67 mV, and the peak current ratios ($i_{p,c}/i_{p,a}$) range between 0.36 and 1.0 (scan rate of 0.1 V s^{-1}; see Table S2† for a summary of the values). Thus, this redox couple is not completely reversible in most cases, as we have previously observed in several related compounds.[30,32] All of these potentials are more negative than the ferrocene/ferrocenium reference potential, showing that these complexes are easily oxidized with their HOMO destabilized by the electron-rich π-donating ligand. The C^Y ligand has minimal effect on the Ir^{IV}/Ir^{III} redox potential. In NacNac^{NMe_2} complexes **1** and **5** and NacNac^{Cy} complexes **2** and **6** the potentials differ by 40 mV and 20 mV, respectively, with the more donating pmb cyclometalating ligand inducing a modest cathodic shift. Moreover, the potentials of all compounds reported here are within 90 mV of the redox potential for the corresponding Ir (ppy)$_2$(NacNac^R) complex with the same NacNac ligand,[30,32] showing that the C^Y ligand has a much subtler effect on the HOMO energy than the NacNac. In short, these trends in Ir^{IV}/Ir^{III} redox potentials are consistent with the idea that the HOMO is largely localized on the NacNac and its energy dictated primarily by the ancillary ligand's substitution pattern. Sweeping cathodically, the first reduction potentials were not clearly determined as they occur near the solvent potential window and are irreversible. In most complexes a peak cathodic potential ($E_{p,c}$) near −3.0 V *vs.* Fc$^+$/Fc is noted, consistent with shallow LUMO levels in these compounds.
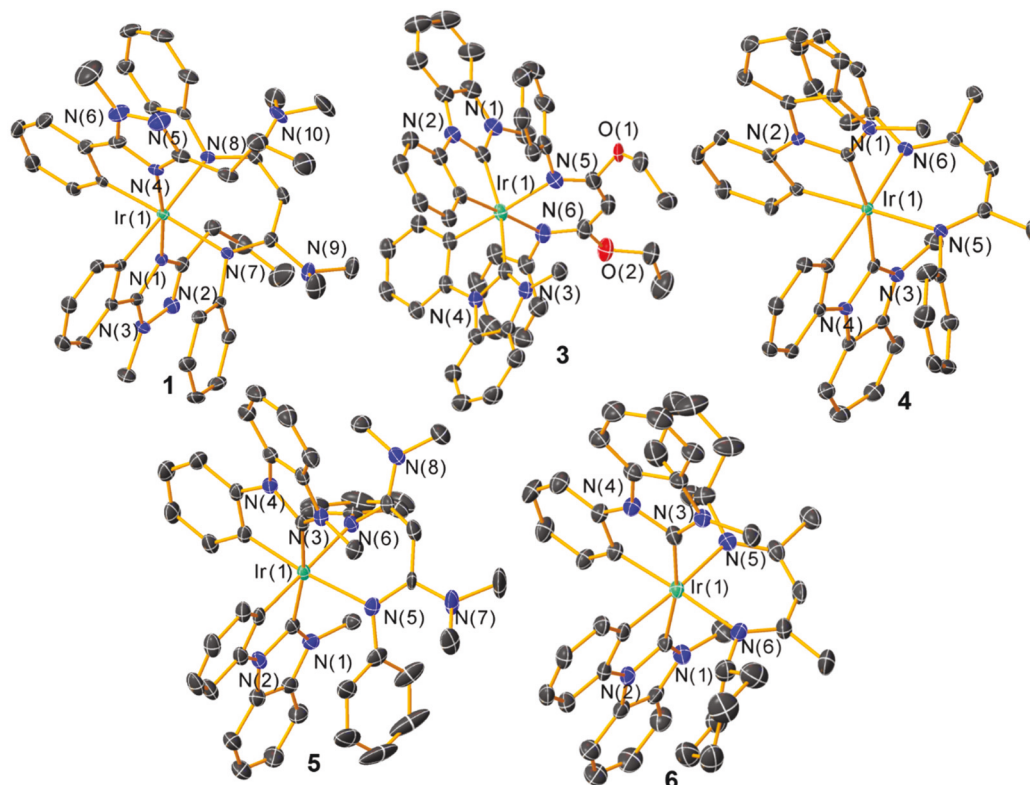

Fig. 2 X-ray crystal structure of complexes **1** and **3**–**6**. Hydrogen and solvent molecules are intentionally omitted.

Table 1 Summary of redox potentials and photophysical properties

| | $E(Ir^{IV}/Ir^{III})/V$ vs. Fc^+/Fc | UV-vis absorption λ/nm ($\varepsilon/10^3$ M^{-1} cm^{-1})[a] | Emission, λ/nm | | Φ_{PL}[a] | τ^a/μs | E_{T1}[d]/eV | $E(Ir^{IV}/{}^*Ir^{III})/V$ vs. Fc^+/Fc |
			293 K[a]	77 K[c]				
1	−0.22	244 (12), 329 (2.4), 380 (1.6)	576	568	0.025	0.13	2.6	−2.8
2	−0.41	245 (29), 321 (sh, 7.0), 375 (5.4)	642	567	0.0032	0.068	2.3	−2.7
3	−0.03	240 (46), 291 (sh), 301 (25), 346 (12)	b	509	b	b	2.4[e]	−2.4
4	−0.16	242 (39), 302 (22), 394 (7.8)	b	529	b	b	2.4[e]	−2.6
5	−0.26	242 (79), 296 (44), 387 (6.2), 430 (4.5)	591	580	0.039	0.85	2.5	−2.8
6	−0.43	296 (19), 304 (sh) (10), 384 (3.9), 439 (0.9)	675	578, 613 (sh)	0.0027	0.12	2.2	−2.6

[a] In MeCN unless otherwise noted. [b] Not luminescent at 293 K. [c] In butyronitrile. [d] Determined from the intersection point of UV-vis absorption and emission unless otherwise noted. [e] Determined from the first vibronic peak in the 77 K emission spectrum.

Photophysical properties

In the UV–vis spectra, in Fig. 3, an intense ligand-centered (LC) $\pi \rightarrow \pi^*$ band is found near 250 nm (40 000 cm^{-1}). Weaker charge-transfer transitions occur in the 400–500 nm region. Complexes **1** and **2** with the ptz C^Y ligand have lower extinction coefficients compared to the pmb-based complexes (**3–6**). The charge-transfer bands in **1** and **2** are similar in energy, with peaks at 380 and 375 nm, respectively, that tail beyond 400 nm into the visible range. The spectra for complexes with C^Y = pmb are not drastically different, although in **4–6** with the more electron-rich NacNac ligands the reduction of the HOMO–LUMO gap manifest as absorption that tails further into the visible region, approaching 500 nm in complex **5**. The higher LUMO levels in these ptz and pmb complexes result in less visible absorption than the respective $Ir(ppy)_2(NacNac^R)$

complexes,[30,32] but in all cases there is absorption beyond 400 nm, making these complexes good candidates for photoredox catalysis under blue-light irradiation.

Photoluminescence spectra are shown in Fig. 4. The Ir (C^Y)$_2$(NacNac^R) complexes are non-emissive or weakly emissive at room temperature; complexes **3** and **4** do not show appreciable photoluminescence, whereas the rest have modest photoluminescence quantum yields (Φ_{PL}) between 0.0027 and 0.039. All complexes are luminescent at 77 K in rigid solvent glass. Normally cyclometalated iridium compounds with C^Y = ptz or pmb luminesce deep in the blue region of the spectrum,[33,34,38,39] but in complexes **1–6** the PL maxima are all in the green to yellow region, centered beyond 500 nm in each case. This large bathochromic shift in the emission spectra is a consequence of the strongly donating NacNac ligands, which destabilize the HOMO and lower the energy of the ^{3}CT state. Consistent with this, there is a clear correlation between redox potential and peak PL wavelength at 77 K. Complex **3**, Ir (pmb)$_2$(NacNac^{OEt}), has the most positive Ir^{IV}/Ir^{III} potential (*i.e.* most stable HOMO) and the lowest PL maximum wave-

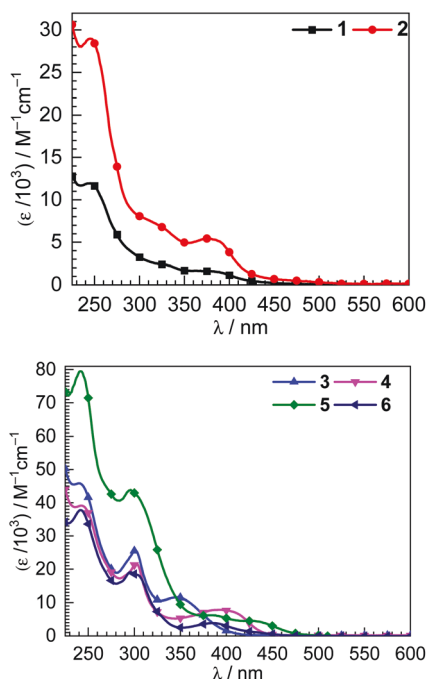**Fig. 3** Overlaid UV-vis spectra of **1**, **2** (top), and **3–6** (bottom), recorded in MeCN at room temperature.
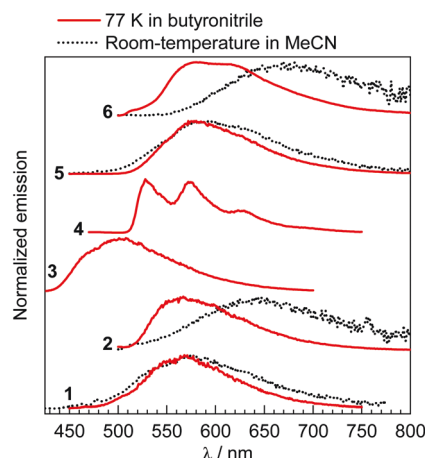

Fig. 4 Overlaid emission spectra of **1–6** at 293 K (black dotted lines) in MeCN and 77 K (red solid lines) in a butyronitrile glass. Complexes **3** and **4** are non-emissive at 293 K. The excitation wavelength (λ_{ex}) is 420 nm for all spectra.

length. In contrast, the potentials for **1**, **2**, **5**, and **6** (NacNac^{NMe_2} and NacNac^{Cy}) are considerably more negative, and their photoluminescence spectra are the most red-shifted. NacNac^{Me} complex **4** has an intermediate value for both the Ir^{IV}/Ir^{III} potential and the emission wavelength. At 77 K the compounds that are also luminescent at room temperature (**1**, **2**, **5**, and **6**) experience a measurable rigidochromic blue shift, which is most pronounced in NacNac^{Cy} complexes **2** and **6**. This pronounced shift is further evidence for substantial excited-state charge-transfer character, as we have documented in many other related compounds.[30,35,37] For the compounds that luminesce at room temperature PL lifetimes were also recorded, and they span the range of 0.068 to 0.85 μs, shorter in the NacNac^{Cy} complexes than the NacNac^{NMe_2} complexes at parity of C^Y ligand. NacNac^{NMe_2} complex **5** has the longest PL lifetime in the series (0.85 μs), in large part due to this compound having the smallest nonradiative rate constant in the series; $k_{nr} = 1.1 \times 10^6$ s^{-1}, smaller than the rest by at least a factor of 7.

DFT calculations

Geometry optimizations and electronic-structures calculations on Ir(pmb)$_2$(NacNac^R) complexes **5** and **6** (R = NMe$_2$ and Cy, respectively) were conducted with continuum MeCN solvation. Crystallographic inputs were used, and the minimized geometries were not appreciably different from the solid-state structures. The results are summarized in Fig. 5. The DFT calculations are in line with the cyclic voltammetry data described above. We observed that the Ir^{IV}/Ir^{III} redox potentials depended significantly on the NacNac substitution pattern, and the computed frontier orbitals reveal that the HOMO has majority NacNac^R character, 59% in **5** (R = NMe$_2$) and 83% in **6** (R = Cy). The HOMO energy also trends with the redox potentials. The computed HOMO energy for NacNac^{NMe_2} complex **5** is

−4.96 eV, destabilized to −4.79 eV in NacNac^{Cy} complex **6**. This 0.17 eV difference perfectly mirrors the 0.17 V difference in ground-state Ir^{IV}/Ir^{III} potentials we observe between these two compounds (Table 1). The computed LUMOs for both compounds are primarily centered on the pmb cyclometalating ligand, as is typically the case for cyclometalated iridium complexes. The reduction waves in the CVs (Fig. S13†) are irreversible and for **6** not particularly well-resolved, but the DFT calculations reveal that the LUMO energies for these two compounds differ by only 0.04 eV, consistent with the minority contribution of the NacNac^R ligand to the LUMO. To further confirm the NacNac-centered character of the HOMO and its participation in the redox chemistry, we computed spin-density plots for the $S = \frac{1}{2}$ radical cations of **5** and **6**, which would form following electron transfer to an acceptor. These plots are shown in Fig. S14,† and while they do indicate some spin delocalization there is pronounced spin density on the NacNac^R ligand, particularly evident in NacNac^{Cy} complex **6**. Finally, the disparate contributions of the HOMO and LUMO, the former being NacNac^R-centered and the latter being pmb-centered, with neither having substantial Ir 5d character, indicates that the HOMO → LUMO transition in these compounds is best described at ligand-to-ligand charge transfer, LL'CT.

Excited-state redox potentials

Estimation of the excited-state redox potential, $E(Ir^{IV}/{*}Ir^{III})$, requires two terms – the ground-state Ir^{IV}/Ir^{III} potential, determined by cyclic voltammetry (see above), and the triplet excited-state energy, E_{T1}. This latter term can be estimated in two ways. For compounds that luminesce at room-temperature, E_{T1} is estimated from the intersection point of the normalized UV-vis absorption and PL spectra, also known as the zero–zero spectroscopic energy, E_{0-0}. For the compounds that only luminesce at 77 K this method is not available, and E_{T1} was esti-
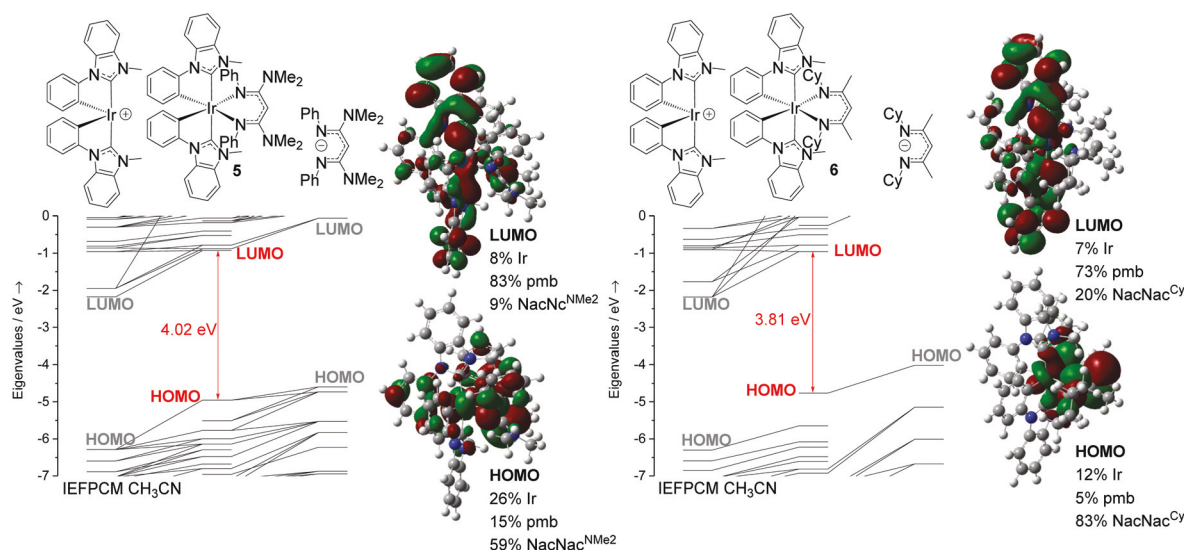

Fig. 5 Frontier Kohn–Sham orbitals of complexes **5** and **6** and associated Mulliken population analysis. Percentages are of orbital density.

mated from the first peak maximum in the 77 K spectrum. The E_{T1} values are included in Table 1. Having previously used both methods to determine E_{T1}, we estimate uncertainty of *ca.* ±0.1 eV for this parameter. To validate our estimation of the triplet excited-state energy, we also used DFT to compute free energies of optimized triplet states for complexes **4–6**, with MeCN solvation. The triplet state energies so computed are 0.1–0.3 eV lower than the experimental values listed in Table 1, but they follow the same general trend for complexes **4–6**. The experimental (2.5 eV) and computed (2.4 eV) E_{T1} values for NacNac^{NMe_2} complex **5** are the highest in this subset, followed by NacNac^{Me} complex **4** (2.4 eV experimental, 2.1 eV computed), and then NacNac^{Cy} complex **6** (2.2 eV experimental, 2.0 eV computed). These results suggest that our E_{T1} estimates are reasonably accurate, and in particular comparisons between compounds in this series are valid.

Using $E(Ir^{IV}/Ir^{III})$ and E_{T1}, eqn (1) provides an estimate of the excited-state potential, $E(Ir^{IV}/*Ir^{III})$.

$$E(Ir^{IV}/*Ir^{III}) = E(Ir^{IV}/Ir^{III}) - E_{T1} \qquad (1)$$

These excited state potentials span a range of −2.4 to −2.8 V *vs.* Fc$^{+/0}$. The −2.8 V Ir^{IV}/*Ir^{III} potentials in NacNac^{NMe_2} complexes **1** and **5** represent the most potent excited state reduction potentials ever recorded for a cyclometalated iridium photoreductant, exceeding the −2.4 to −2.6 V range of Ir(ppy)$_2$(NacNac^R) complexes.[30,32] This cathodic shift in excited-state redox potential is primarily caused by the increase in triplet energy, E_{T1}, upon replacing ppy with ptz or pmb. Specifically, the E_{T1} value in Ir(ppy)$_2$(NacNac^{NMe_2}) (**7**) is 2.3 eV, which increases to 2.6 and 2.5 eV in the ptz and pmb analogues, **1** and **5**. For all complexes reported here, the E_{T1} values are the same as (**3** and **4**) or 0.2 to 0.3 eV higher than (**1**, **2**, **5**, and **6**) the corresponding Ir(ppy)$_2$(NacNac^R) complex.

Stern–Volmer quenching studies

To determine whether the increased thermodynamic driving force for photoinduced electron transfer correlates with faster kinetics for photoinduced electron-transfer reactions, we conducted Stern–Volmer quenching experiments on two electron-acceptor substrates. NacNac^{NMe_2} complexes **1** and **5** were chosen for this study because they have not only the most negative Ir^{IV}/*Ir^{III} potentials, but also higher photoluminescence quantum yields and longer lifetimes than others to facilitate Stern–Volmer studies. The two quenchers we used were benzophenone (E(BP/BP$^{•−}$) = −2.11 V *vs.* Fc$^{+/0}$) and acetophenone (E(AP/AP$^{•−}$) = −2.51 V *vs.* Fc$^{+/0}$),[40] which have reduction potentials close to the excited-state potentials of the complexes. PL spectra and decay traces for the quenching experiments, used to determine data points for the Stern–Volmer plots in Fig. 6, are collected in Fig. S15–S21 of the ESI.† For experiments with benzophenone as the quencher both steady-state and time-resolved emission data were collected, allowing us to distinguish static and dynamic quenching.[41] Fig. 6a, where the steady-state and time-resolved data overlay very well, shows that dynamic quenching is occurring.
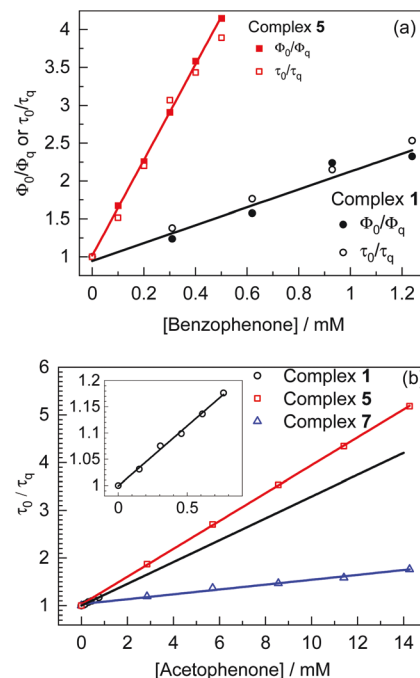

Fig. 6 (a) Stern–Volmer plots for complexes **1** and **5** with benzophenone as the quencher, recorded at 293 K in MeCN solvent. Steady-state (filled symbol) and time-resolved emission (hollow symbol) data are both shown, with λ_{ex} = 420 nm for steady-state emission and 453 nm for time-resolved emission. (b) Comparison of Stern–Volmer plots (time-resolved emission) of complexes **1** (black circles), **5** (red squares), and **7** (blue triangles) with acetophenone as the quencher. The quenching for complex **1** was conducted over a much smaller concentration range, and the inset reproduces those data with the same axis labels.

Fig. 6b overlays quenching data for **1**, **5**, and **7** (C^Y = ppy) with acetophenone, measured *via* time-resolved emission only. From the Stern–Volmer plots in Fig. 6 the bimolecular rate constant for photoinduced electron transfer can be found by dividing the slope of each plot (often denoted as K_{SV}) by the photoluminescence lifetime of the photosensitizer (τ_0). The quenching rate constants are listed in Table 2, and they are substantially larger for new complexes **1** and **5** compared to *fac*-Ir(ppy)$_3$ (**10**) and Ir(ppy)$_2$(NacNac^{NMe_2}) (**7**).

Table 2 Summary of excited-state electron-transfer parameters, measured in MeCN solution

Complex	E(Ir^{IV}/*Ir^{III})^a/V	$k_q \times 10^{-9}$/M^{-1} s^{-1} BP^b	AP^c
Ir(ptz)$_2$(NacNac^{NMe_2}) (**1**)	−2.8	9.6	2.3
Ir(pmb)$_2$(NacNac^{NMe_2}) (**5**)	−2.8	6.9	0.34
Ir(ppy)$_2$(NacNac^{NMe_2}) (**7**)	−2.6	5.6^d	0.068
fac-Ir(ppy)$_3$ (**10**)	−2.1	1.9^d	N.D.

^{a} Referenced to Fc$^+$/Fc. ^{b} Benzophenone quencher. ^{c} Acetophenone quencher. ^{d} Previously reported in ref. 32.

3258 | *Inorg. Chem. Front.*, 2021, **8**, 3253–3265

This journal is © the Partner Organisations 2021

Photocatalytic hydrodehalogenation

Complex **5** was evaluated as a photocatalyst for the hydrodehalogenation of bromide and chloride substrates. We used conditions similar to those developed previously, with 1,3-dimethyl-2,3-dihydro-2-phenyl-benzimidazole (BIH) as the sacrificial reagent.[30,31] As shown in Fig. 7, the hydrodehalogenation of 1-bromo-4-phenylbutane proceeded to quantitative conversion, producing a 2:1 ratio of the straight-chain product *n*-butylbenzene and the cyclized product tetralin. The latter product forms *via* intramolecular radical addition to the phenyl ring subsequent to cleavage of the C–Br bond, as we have observed previously with the same substrate[31] and others have seen with related but more complex substrate classes.[42,43] For the aryl chloride substrate 4-chloro methylbenzoate, clean hydrodehalogenation was observed, albeit with a modest product yield of 39%. This outcome suggested the possibility that complex **5** was degrading during the catalytic reaction, motivating us to screen several solvents, and as shown in Fig. S22† dimethylacetamide (DMA) turned out to be the best solvent. We also evaluated complex **5** as a catalyst for the photocatalytic hydrodebromination of 1-bromoadamantane, in comparison with $Ir(ppy)_2(NacNac^{NMe_2})$ (**7**) and *fac*-$Ir(ppy)_3$ (**10**) (Fig. S23†). Complex **5** (yield of 38%) outperforms *fac*-$Ir(ppy)_3$ (yield of 24%), although both fall well short of the yields observed with complex **7** (91%).[31] Finally, in the hydrodehalogenation of 1-chloro-4-phenylbutane, we observed low conversion even during prolonged reaction times (Fig. S24†). After 72 h we observed the formation of 10% of *n*-butylbenzene, along with some unidentified side products. These preliminary screens show that the more highly reducing complex **5** is active for the photocatalytic hydrodehalogenation of challenging halide substrates, although for the few transformations we studied there are no obvious benefits of this modified catalyst over the top-performing $Ir(ppy)_2(NacNac^R)$ catalysts we previously described.
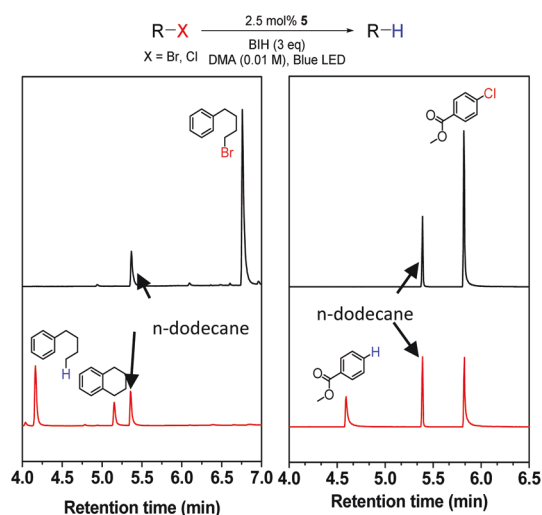

Fig. 7 GC traces showing the hydrodehalogenation of an alkyl bromide (left) and aryl chloride (right) substrate, using **5** as the photocatalyst.

Discussion

In this study, we unveiled a strategy for further improving the excited-state redox potentials of bis-cyclometalated iridium photosensitizers. We had previously disclosed a number of $Ir(ppy)_2(NacNac^R)$ photosensitizers with variable NacNac substitution, and all of these had excited-state redox potentials, $E(Ir^{IV}/{^*}Ir^{III})$, more negative than *fac*-$Ir(ppy)_3$ but all quite similar to one another. We had previously attempted replacing the ppy cyclometalating ligand with either a substituted variant, 2-(4-*tert*-butylphenyl)pyridine (tbppy), or with 1-phenylpyrazole (ppz),[30] but neither of these substitutions was successful at either shifting the excited-state potential more negative or improving photoredox catalysis outcomes. We disclose in this work that a way to push this excited-state potential to even more negative values is to use either triazole or NHC-based cyclometalating ligands. Specifically, we used the triazole-based C^Y ligand ptz and the NHC-based C^Y ligand pmb, introduced by Lo *et al.*[33] and Sajoto *et al.*[34] in blue-phosphorescent, homoleptic tris-cyclometalated iridium complexes. These homoleptic compounds can only be excited in the UV region, but the substantial HOMO destabilization brought on by the NacNac ligand reduces the HOMO–LUMO gap and enables visible excitation for these heteroleptic $Ir(C^Y)_2(NacNac^R)$ complexes.

In all the $Ir(C^Y)_2(NacNac^R)$ complexes we have studied the HOMO is primarily localized on the NacNac ligand, which is evident from cyclic voltammetry studies and confirmed by the DFT calculations described here. The energetic consequence of using ptz or pmb as the cyclometalating ligand is to destabilize the LUMO, which in turn increases the HOMO–LUMO gap and raises the triplet excited-state energy, E_{T1}. Since the Ir^{IV}/Ir^{III} potentials are minimally altered, but E_{T1} in most cases is significantly increased, according to eqn (1) this results in a more negative excited-state potential. Fig. 8 summarizes structure–property relationships for the 10 compounds shown in Fig. 1. For most of the compounds, in particular the compounds with C^Y = ppy, there is an inverse relationship between the two terms in eqn (1). For compounds with higher

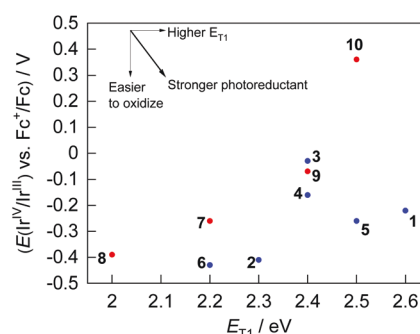**Fig. 8** A plot of the ground-state oxidation potential, $E(Ir^{IV}/Ir^{III})$, *vs.* the excited-state energy, E_{T1}, for compounds **1–6** (blue points) and four previously-described iridium photosensitizers, $Ir(ppy)_2(NacNac^R)$ (**7–9**) and *fac*-$Ir(ppy)_3$ (**10**) (red points).

This journal is © the Partner Organisations 2021

Inorg. Chem. Front., 2021, **8**, 3253–3265 | **3259**

excited-state energies, E_{T1}, the ground-state redox potential is more positive. However, in the new compounds described here with C^Y = ptz or pmb, in particular **1** and **5**, this scaling relationship is avoided and E_{T1} values comparable to *fac*-Ir (ppy)$_3$ are obtained, but with ground-state Ir^{IV}/Ir^{III} potentials that are substantially more negative.

As a result, the compounds described in this work are among the most potent visible-light photoreductants ever reported, in particular complexes **1**, **2**, and **5**. The −2.8 V Ir^{IV}/ *Ir^{III} potentials in complexes **1** and **5** are comparable to the potentials of a series of homoleptic W(CNAr)$_6$ complexes reported by Sattler *et al.*[25,44] and are slightly more negative than a class of homoleptic Mo compounds with bidentate isocyanide supporting ligands, studied by Wenger's group.[26,27] They do fall just short of the −3.0 to −3.2 V potentials found in a series of pincer PNP-copper complexes popularized by the groups of Fu and Peters,[45,46] one of which mainly absorbs in the UV but nonetheless has become prominent in photoredox catalysis.[46]

With the improved excited-state reduction potentials realized, we also assessed the kinetics of excited-state electron transfer to ketone acceptors. Benzophenone and acetophenone are both difficult to reduce, with reduction potentials similar to the excited-state potentials of many iridium photoreductants, so improving the electron-transfer driving force could have a large impact on the quenching rate constants. We can exclude the possibility of an energy transfer mechanism in these quenching reactions. The triplet energies of benzophenone (3.0 eV) and acetophenone (3.2 eV)[47] are substantially higher than **1** (2.6 eV) and **5** (2.5 eV), precluding triplet energy transfer. The measured quenching rate constants are listed in Table 2, and all fall below the diffusion limit in acetonitrile, *ca.* 2–4 × 10^{10} in MeCN.[48,49] The driving force of photoinduced electron transfer is the difference between the excited-state potential and reduction potential of the quenching molecule. For the quenching reaction between **1** and BP, 0.7 V of driving force leads to a quenching rate close to the diffusion limit. Though not a perfect comparison due to different solvent systems, the rate constants observed here are similar to the quenching rate constants observed with tungsten-based photoreductants.[25] Comparison of the quenching rates in Table 2, which includes complexes **1** and **5**, their C^Y = ppy analogue **7**, and *fac*-Ir(ppy)$_3$ (**10**), we see that the quenching rate constants scale directly with the excited-state reducing power of the photosensitizer, suggesting electron-transfer is occurring in the Marcus-normal region. The fastest electron-transfer quenching was observed with Ir(ptz)$_2$(NacNac^{NMe_2}) (**1**), and with benzophenone as the quencher we observe that the increased driving force in **1** leads to a 5-fold increase in quenching rate constant relative to *fac*-Ir(ppy)$_3$, and a 1.7-fold increase relative to Ir(ppy)$_2$(NacNac^{NMe_2}) (**7**). The effect is magnified with acetophenone as the quencher, which is even more difficult to reduce. The quenching rate constant for **1** with acetophenone is 34 times higher than that of complex **7**. We do note that even though the excited-state reduction potentials of C^Y = ptz complex **1** and C^Y = pmb complex **5** are nomin-

ally the same, at −2.8 V, the quenching rate constants for complex **1** are all notably larger. This may be because there is a ±0.1 V uncertainty in the excited-state potential, primarily arising from estimation of E_{T1}, such that the excited-state potentials of **1** and **5** are not actually identical. Regardless of the precise origin, the quenching rate constants for complex **5** are still larger than *fac*-Ir(ppy)$_3$ and **7**.

The photocatalytic hydrodehalogenation studies show that complex **5** can activate halide substrates, though with the aryl chloride substrate 4-chloro methylbenzoate and the alkyl bromide substrate 1-bromoadamantane full conversion was not achieved, suggesting decomposition of the catalyst during the reaction. Thus, for the reactions reported here we do not see a clear advantage of **5** in catalysis, relative to our previously reported NacNac-based photosensitizers. However, we are continuing to develop photoredox reactions on challenging substrates enabled by strongly reducing iridium photosensitizers. Given their potent excited-state reduction potentials and fast photoinduced electron transfer rates newly developed complexes **1** and **5** remain good candidates for these future studies.

Conclusions

To improve the excited-state reducing ability of bis-cyclometalated iridium NacNac photoreductants, we have replaced the typical 2-phenylpyridine cyclometalating ligands with triazole (ptz) and NHC (pmb) variants. The HOMO energy levels of these complexes are mainly determined by the NacNac ancillary ligands, but the LUMO and the excited-state energy levels can be augmented with these alternative cyclometalating ligands. The elevation of the excited-state energy (E_{T1}) results in more negative excited-state potentials by up to 400 mV relative to our previously discovered complexes. The −2.8 V excited-state potential observed in two of the complexes denotes them as the most photoreducing iridium photosensitizers ever reported, and their rates of photoinduced electron transfer also exceed those of other iridium photosensitizers. Finally, we have shown the effective hydrodehalogenation of alkyl and aryl halide substrates with complex **5** under blue LED irradiation, demonstrating that the high reducing ability of this compound can lead to photocatalysis on challenging substrates. This work highlights that with appropriate ligand-design strategies it is possible to further optimize the excited-state redox chemistry of iridium photoreductants, opening the door to an enticing new class of photosensitizer molecules for catalysis applications.

Experimental section

Materials

All reactions are performed or prepared in a nitrogen-filled glove box operating at <1 ppm of O$_2$ and <1 ppm of H$_2$O. Solvents for reactions and photophysical measurements were

3260 | *Inorg. Chem. Front.*, 2021, **8**, 3253–3265

This journal is © the Partner Organisations 2021

dried by the method of Grubbs with a commercial solvent purification system (SPS) and stored over 3 Å molecular sieves. Anhydrous butyronitrile for low-temperature emission was purchased from Aldrich. All NMR solvents were dried and stored over 3 Å molecular sieves. The β-diketiminate ligands NacNac^{R}H, and their alkali salts NacNac^{NMe_2}K, NacNac^{Cy}Li, NacNac^{OEt}K, and NacNac^{Me}K were prepared according to our previously reported procedures.[30,32,35] The C^Y ligand precursors, 1-methyl-3-propyl-5-phenyl-1H-1,2,4-triazole (ptz) and 1-phenyl-3-methylbenzimidazolium iodide (pmb) and their chloro-bridged iridium dimer $[Ir(C^\wedge Y)_2(\mu\text{-}Cl)]_2$ (C^Y = ptz, pmb) were prepared according to the literature procedures.[33,34] The quenching reagents benzophenone and acetophenone were purchased from Aldrich and used without further purification.

Physical methods

JEOL ECX-400P, ECA-500, and ECA-600 NMR spectrometers were used to record the NMR spectra at room temperature. For optical measurements, UV–vis absorption spectra were recorded in acetonitrile solution at room temperature with screw-capped quartz cuvettes and an Agilent 8454 UV–vis spectrophotometer. A Horiba FluoroMax-4 spectrofluorometer was used to measure the emission spectra using an appropriate long-pass filter to cut off the excitation light from the detector. For room-temperature emission, 1 cm quartz cuvettes with septum-sealed screw caps were used. A custom quartz EPR tube with a Teflon valve was immersed in a liquid nitrogen-filled finger dewar to obtain low-temperature emission. Photoluminescence quantum yields (Φ_{PL}) were measured relative to tetraphenylporphyrin (Φ_{PL} = 0.11 in toluene) by using the equation, $\Phi_x = \Phi_{ref} \times (\text{slope}_x/\text{slope}_{ref}) \times (\eta_{MeCN}/\eta_{toluene})^2$, where the slope comes from the best-fit line of the integrated area of collected emission $vs.$ absorbance at the excitation wavelength. The refractive index (η) of the solvents is 1.3441 for MeCN and 1.4969 for toluene. Luminescence lifetimes were measured with a Horiba DeltaFlex Lifetime System, using 390 nm and 453 nm pulsed diode excitation with appropriate wavelength filters and neutral density filters. The emission decays were fit by using the instrument analysis software to obtain lifetimes. For electrochemical properties, cyclic voltammetry (CV) measurements were performed with a CH Instruments 602E potentiostat interfaced with an inert-atmosphere glovebox via wire feedthroughs. Samples were dissolved in acetonitrile or propylene carbonate with 0.1 M TBAPF$_6$ as a supporting electrolyte. A 3 mm diameter glassy carbon working electrode, a platinum wire counter electrode, and a silver wire pseudo-reference electrode were used. Potentials were referenced to an internal standard of ferrocene.

Stern–Volmer quenching studies

All blank and stock solutions were prepared in a glove box to avoid oxygen quenching. Stock solutions of the iridium complexes, benzophenone, and acetophenone were prepared in dry MeCN solvent. The iridium complex was diluted in a quartz cuvette to make a 1.0–3.0 × 10^{-6} M solution, ensuring the

absorbance at the excitation wavelength was less than 0.1. After measuring room-temperature emission and photoluminescence lifetime, 5–10 µL of quencher solution was added via microsyringe to the cuvette for the next measurement. The concentration of the quencher stock solution was between 2.0 and 3.0 × 10^{-3} M. UV–vis absorption spectra, photoluminescence lifetimes, and room-temperature emission spectra were recorded after every addition of quencher aliquot. For lifetime measurements the samples were excited at 453 nm, and for steady-state emission spectra, 420 nm excitation was used. Also, to rule out any quenching by adventitious oxygen, the emission spectra and lifetime were measured repeatedly after the addition of the quencher to ensure stable values.

Photoredox catalysis

Detailed procedures for photoredox reactions can be found in other published work from our group.[31] Reagents were measured and combined in an inter atmosphere inside the glovebox. A stock solution of the catalyst, **Ir5**, and the sacrificial reagent was prepared. A 1 mL aliquot of this stock solution was used to dissolve 10 µmol of the substrate, ensuring 2.5 mol% loading of the iridium catalyst and 3 equiv. of sacrificial reagent. The vial was sealed with a screw-cap and removed from the glovebox. The vial was irradiated in a home-built photoreactor surrounded by blue (465–470 nm) LED Flex Ribbon Strips purchased from Creativelighting. The reaction progress was tracked with gas chromagraphy.

DFT calculations

Static and time-resolved density-functional theory calculations were performed using the Gaussian 16 software package.[50] Initial structures for geometry optimization were taken from crystal structures and optimized using the hybrid PBE1 functional and the TZVP basis set, for H, C, and N atoms, and the SDD effective core potential and basis set for Ir.[51,52] Calculations on diamagnetic compounds were spin-restricted; those on radicals were spin-unrestricted. Harmonic frequency calculations confirmed optimized structures to be potential energy minima. Geometry optimizations and single-point calculations incorporated IEFPCM solvation in acetonitrile.[53–55] The AOMix program was utilized for population analysis.[56,57]

General procedure 1 for the preparation of bis-cyclometalated iridium β-diketiminate complexes (1, 3, 4, and 5)

In a glovebox, the chloro-bridged dimer $[Ir(C^\wedge Y)_2(\mu\text{-}Cl)]_2$ was suspended in 2 mL of THF, and 2.1 equivalents of the respective NacNac^R potassium salt was dissolved in 6 mL of THF. The solution of the NacNac ligand was added to the chloro-bridged dimer suspension via a pipet. The mixture was stirred for 1 h at room temperature, during which the color darkened from yellow to orange or red. The solution was concentrated in $vacuo$, and the crude product was extracted into 2 mL of toluene and filtered. The solution was again concentrated, and trituration with 2 mL of diethyl ether released the solid

This journal is © the Partner Organisations 2021

Inorg. Chem. Front., 2021, **8**, 3253–3265 | **3261**

product, which was washed with 2 × 2 mL of pentane and dried under vacuum.

General procedure 2 for the preparation of bis-cyclometalated iridium β-diketiminate complexes (2 and 6)

In a glovebox, the chloro-bridged dimer $[Ir(C^\wedge Y)_2(\mu\text{-Cl})]_2$ was suspended in 2 mL of toluene, and 2.1 equivalents of the NacNac^{Cy} lithium salt (NacNac^{Cy}Li) was dissolved in 6 mL of toluene and added to a pressure tube with a Teflon-lined cap. The tube was taken out from the glovebox to the benchtop. Then, the mixture was stirred for 12 h at 110 °C, during which time the color darkened, and a precipitate formed. The crude product was extracted into 2 mL of THF and filtered, followed by removal of the solvent *in vacuo*. The resulting solid was washed with diethyl ether to remove the salt byproduct, and the remaining solid was washed with 2 × 2 mL of pentane and dried under vacuum.

Preparation of Ir(ptz)$_2$(NacNac^{NMe_2}), (1). Prepared by general procedure 1 using $[Ir(ptz)_2(\mu\text{-Cl})]_2$ (100 mg, 1 equiv., 0.0796 mmol) and NacNac^{NMe_2}K (58 mg, 2.1 equiv., 0.17 mmol) yield: 85 mg (59%). ^{1}H NMR (400 MHz, benzene-d_6) δ 6.71–6.56 (m, 12H), 6.49 (t, J = 7.3 Hz, 2H), 6.28–6.14 (m, 4H), 4.29 (s, 1H), 3.49–3.41 (m, 2H), 3.30 (s, 6H), 3.13 (dt, J = 15.9, 7.7 Hz, 2H), 2.31 (d, J = 2.9 Hz, 12H), 2.15 (pent, J = 7.5 Hz, 4H), 1.14 (t, J = 7.3 Hz, 6H). ^{13}C{^{1}H} NMR (126 MHz, benzene-d_6) δ 165.9, 165.5, 161.4, 156.0, 152.9, 133.9, 133.0, 128.4, 126.9, 125.9, 123.4, 119.9, 119.3, 79.7, 41.4, 36.7, 28.8, 21.1, 14.4. UV–vis (MeCN) λ/nm (ε/M^{-1} cm^{-1}) 244 (12 000), 329 (2400), 380 (1600).

Preparation of Ir(ptz)$_2$(NacNac^{Cy}), (2). Prepared by general procedure 2 using $[Ir(ptz)_2(\mu\text{-Cl})]_2$ (100 mg, 1 equiv., 0.0796 mmol) and NacNac^{Cy}Li (51 mg, 2.1 equiv., 0.17 mmol) yield: 70 mg (46%). ^{1}H NMR (400 MHz, benzene-d_6) δ 7.03 (d, J = 7.0 Hz, 2H), 6.76–6.66 (m, 6H), 4.33 (s, 1H), 3.43 (s, 6H), 3.28 (t, J = 12.1 Hz, 2H), 3.11 (dt, J = 15.9, 7.8 Hz, 2H), 2.08 (h, J = 7.5 Hz, 4H), 1.95 (s, 6H), 1.82 (d, J = 12.1 Hz, 2H), 1.65–1.55 (m, 2H), 1.55–1.45 (m, 2H), 1.44–1.37 (m, 2H), 1.26 (t, J = 13.7 Hz, 4H), 1.12 (t, J = 7.4 Hz, 6H), 0.76 (m, 6H), 0.51 (t, J = 12.7 Hz, 2H), 0.29 (d, J = 12.4 Hz, 2H). ^{13}C{^{1}H} NMR (126 MHz, benzene-d_6) δ 165.7, 162.3, 158.4, 157.6, 133.6, 133.4, 129.0, 128.0, 127.8, 127.6, 123.7, 119.8, 100.0, 66.7, 36.8, 34.8, 33.6, 28.6, 26.8, 26.8, 26.3, 25.4, 21.4, 14.3. UV–vis (MeCN) λ/nm (ε/M^{-1} cm^{-1}) 245 (29 000), 321 (sh, 7000), 375 (5400).

Preparation of Ir(pmb)$_2$(NacNac^{OEt}), (3). Prepared by general procedure 1 using $[Ir(pmb)_2(\mu\text{-Cl})]_2$ (100 mg, 1 equiv., 0.0779 mmol) and NacNac^{OEt}K (57 mg, 2.1 equiv., 0.16 mmol) yield: 94 mg (66%). ^{1}H NMR (500 MHz, benzene-d_6) δ 7.59 (d, J = 7.8 Hz, 2H), 7.04 (dt, J = 21.5, 7.6 Hz, 8H), 6.53 (ddt, J = 23.3, 16.4, 7.9 Hz, 10H), 6.30 (t, J = 7.4 Hz, 2H), 6.16 (s, 4H), 4.33 (s, 6H), 4.22 (s, 1H), 3.69 (m, 4H), 0.78 (t, J = 7.0 Hz, 6H). ^{13}C{^{1}H} NMR (151 MHz, methylene chloride-d_2) δ 189.0, 163.3, 148.8, 148.0, 139.9, 137.8, 136.8, 132.6, 125.8, 123.5, 123.2, 123.0, 121.4, 119.6, 111.5, 111.4, 111.0, 110.8, 110.3, 64.7, 14.6. UV–vis (MeCN) λ/nm (ε/M^{-1} cm^{-1}) 240 (46 000), 301 (25 000), 346 (12 000).

Preparation of Ir(pmb)$_2$(NacNac^{Me}), (4). Prepared by general procedure 1 using $[Ir(pmb)_2(\mu\text{-Cl})]_2$ (100 mg, 1 equiv., 0.0779 mmol) and NacNac^{Me}K (47 mg, 2.1 equiv., 0.16 mmol). Dichloromethane was used to extract the product, which was washed with diethyl ether and pentane. Yield: 88 mg (66%). ^{1}H NMR (500 MHz, chloroform-d) δ 7.89 (d, J = 8.2 Hz, 2H), 7.60 (d, J = 7.9 Hz, 2H), 7.39 (dt, J = 25.3, 7.5 Hz, 4H), 6.99 (d, J = 7.7 Hz, 2H), 6.55 (d, J = 8.2 Hz, 2H), 6.48–6.38 (m, 6H), 6.24 (d, J = 8.7 Hz, 2H), 6.08 (d, J = 4.0 Hz, 4H), 5.21 (s, 2H), 4.63 (s, 1H), 4.57 (s, 6H), 1.50 (s, 6H). ^{13}C{^{1}H} NMR (151 MHz, THF-d_8) δ 190.4, 157.8, 153.1, 149.1, 141.3, 139.1, 137.8, 133.6, 127.2, 126.9, 126.1, 124.7, 123.9, 123.8, 122.6, 122.5, 120.0, 112.0, 111.9, 111.0, 98.0, 33.2. UV–vis (MeCN) λ/nm (ε/M^{-1} cm^{-1}) 242 (39), 302 (22), 394 (7.8).

Preparation of Ir(pmb)$_2$(NacNac^{NMe_2}), (5). Prepared by general procedure 1 using $[Ir(pmb)_2(\mu\text{-Cl})]_2$ (100 mg, 1 equiv., 0.0779 mmol) and NacNac^{NMe_2}K (55 mg, 2.1 equiv., 0.16 mmol) yield: 72 mg (52%). ^{1}H NMR (600 MHz, benzene-d_6) δ 7.70 (d, J = 8.0 Hz, 2H), 7.54 (d, J = 8.1 Hz, 2H), 6.97 (t, J = 7.6 Hz, 2H), 6.92 (t, J = 7.7 Hz, 2H), 6.86 (d, J = 7.0 Hz, 4H), 6.77 (d, J = 8.0 Hz, 2H), 6.72 (t, J = 7.7 Hz, 4H), 6.56 (t, J = 7.4 Hz, 2H), 6.43 (d, J = 8.0 Hz, 4H), 6.34 (t, J = 7.3 Hz, 2H), 3.95 (s, 1H), 3.63 (s, 6H), 2.16 (s, 12H). ^{13}C{^{1}H} NMR (126 MHz, benzene-d_6) δ 169.7, 157.8, 149.0, 139.0, 138.2, 136.4, 132.8, 124.8, 124.2, 122.6, 121.6, 120.6, 119.0, 112.3, 111.1, 109.5, 85.9, 53.0, 40.5, 33.0. One peak is overlapped with the solvent peak and not observed. UV–vis (MeCN) λ/nm (ε/M^{-1} cm^{-1}) 242 (79 000), 296 (44 000), 387 (6200), 430 (4500).

Preparation of Ir(pmb)$_2$(NacNac^{Cy}), (6). Prepared by general procedure 2 using $[Ir(ptz)_2(\mu\text{-Cl})]_2$ (100 mg, 1 equiv., 0.0779 mmol) and NacNac^{Cy}Li (46 mg, 2.1 equiv., 0.17 mmol) yield: 70 mg (52%). ^{1}H NMR (600 MHz, methylene chloride-d_2) δ 8.11–8.09 (m, 2H), 7.59 (d, J = 7.8 Hz, 2H), 7.55–7.52 (m, 2H), 7.39–7.36 (m, 4H), 6.77 (td, J = 7.5, 1.6 Hz, 2H), 6.39–6.29 (m, 4H), 4.28 (s, 6H), 4.02 (s, 1H), 2.90 (td, J = 10.9, 9.7, 6.0 Hz, 2H), 1.78 (s, 6H), 1.45 (d, J = 11.8 Hz, 2H), 1.28–1.23 (m, 3H), 1.18 (dt, J = 12.8, 6.3 Hz, 2H), 1.06 (d, J = 13.0 Hz, 2H), 0.88 (d, J = 13.1 Hz, 2H), 0.66–0.56 (m, 3H), 0.47 (d, J = 12.2 Hz, 2H), 0.31–0.22 (m, 2H), −0.17 (d, J = 13.3 Hz, 3H). ^{13}C{^{1}H} NMR (151 MHz, methylene chloride-d_2) δ 190.6, 159.2, 149.2, 141.9, 137.4, 137.1, 132.8, 129.0, 124.0, 123.0, 122.0, 120.1, 111.8, 111.1, 110.1, 100.2, 68.0, 65.7, 33.5, 33.3, 32.8, 26.7, 26.4, 26.2, 24.5, 15.2. UV–vis (MeCN) λ/nm (ε/M^{-1} cm^{-1}) 296 (19 000), 304 (sh) (10 000), 384 (3900), 439 (9000).

X-ray crystallography details

Single crystals were grown by vapor diffusion of pentane into concentrated toluene or benzene solutions. Crystals were mounted on a Bruker Apex II three-circle diffractometer using MoKα radiation (λ = 0.71073 Å). The data was collected at 123 (2) K and was processed and refined within the APEXII software. Structures were solved by direct methods in SHELXS and refined by standard difference Fourier techniques in the program SHELXL.[58] Hydrogen atoms were placed in calculated positions using the standard riding model and refined isotropically; all non-hydrogen atoms were refined anisotropically.

3262 | *Inorg. Chem. Front.*, 2021, **8**, 3253–3265

This journal is © the Partner Organisations 2021

The structures of **3**, **5**, and **6** all contained heavily-disordered solvent electron density that could not be satisfactorily modelled, necessitating the use of the SQUEEZE function in PLATON.[59] In the structure of **1** one of the propyl groups was disordered, **3** had a disordered ethoxy group, and **4** included a disordered pentane solvate. All were modelled as two-part positional disorders, with distance restraints (SADI) used to affix 1,2 and 1,3 distances in the disordered parts, and rigid bond restraints (SIMU and DELU) for their ellipsoid parameters. Crystallographic details are summarized in Table S1 of the ESI.†

Author contributions

Jong-Hwa Shon: conceptualization, formal analysis, investigation, visualization, writing – original draft, writing – review & editing. Dooyoung Kim: Formal analysis, investigation, writing – review & editing. Thomas G. Gray: Formal analysis, funding acquisition, investigation, visualization, writing – review & editing. Thomas S. Teets: Conceptualization, formal analysis, funding acquisition, project administration, supervision, visualization, writing – original draft, writing – review & editing.

Conflicts of interest

There are no conflicts to declare.

Acknowledgements

Notes and references

1 C. K. Prier, D. A. Rankic and D. W. C. MacMillan, Visible Light Photoredox Catalysis with Transition Metal Complexes: Applications in Organic Synthesis, *Chem. Rev.*, 2013, **113**, 5322–5363.

2 H. Seo, M. H. Katcher and T. F. Jamison, Photoredox activation of carbon dioxide for amino acid synthesis in continuous flow, *Nat. Chem.*, 2016, **9**, 453–456.

3 M. Chen, M. Zhong and J. A. Johnson, Light-Controlled Radical Polymerization: Mechanisms, Methods, and Applications, *Chem. Rev.*, 2016, **116**, 10167–10211.

4 T. R. Cook, D. K. Dogutan, S. Y. Reece, Y. Surendranath, T. S. Teets and D. G. Nocera, Solar Energy Supply and Storage for the Legacy and Nonlegacy Worlds, *Chem. Rev.*, 2010, **110**, 6474–6502.

5 T. S. Teets and D. G. Nocera, Photocatalytic hydrogen production, *Chem. Commun.*, 2011, **47**, 9268.

6 D. A. Nagib and D. W. C. MacMillan, Trifluoromethylation of arenes and heteroarenes by means of photoredox catalysis, *Nature*, 2011, **480**, 224–228.

7 E. B. Corcoran, M. T. Pirnot, S. Lin, S. D. Dreher, D. A. DiRocco, I. W. Davies, S. L. Buchwald and D. W. C. MacMillan, Aryl amination using ligand-free Ni(ɪɪ) salts and photoredox catalysis, *Science*, 2016, **353**, 279–283.

8 J. D. Nguyen, E. M. D'Amato, J. M. R. Narayanam and C. R. J. Stephenson, Engaging Unactivated Alkyl, Alkenyl and Aryl Iodides in Visible-Light-Mediated Free Radical Reactions, *Nat. Chem.*, 2012, **4**, 854.

9 J. D. Nguyen, B. S. Matsuura and C. R. J. Stephenson, A Photochemical Strategy for Lignin Degradation at Room Temperature, *J. Am. Chem. Soc.*, 2014, **136**, 1218–1221.

10 J. W. Beatty and C. R. J. Stephenson, Amine Functionalization via Oxidative Photoredox Catalysis: Methodology Development and Complex Molecule Synthesis, *Acc. Chem. Res.*, 2015, **48**, 1474–1484.

11 C. Dai, J. M. R. Narayanam and C. R. J. Stephenson, Visible-light-mediated conversion of alcohols to halides, *Nat. Chem.*, 2011, **3**, 140–145.

12 A. Arora and J. D. Weaver, Visible Light Photocatalysis for the Generation and Use of Reactive Azolyl and Polyfluoroaryl Intermediates, *Acc. Chem. Res.*, 2016, **49**, 2273–2283.

13 T. P. Yoon, M. A. Ischay and J. Du, Visible light photocatalysis as a greener approach to photochemical synthesis, *Nat. Chem.*, 2010, **2**, 527–532.

14 H. Huo, X. Shen, C. Wang, L. Zhang, P. Röse, L.-A. Chen, K. Harms, M. Marsch, G. Hilt and E. Meggers, Asymmetric photoredox transition-metal catalysis activated by visible light, *Nature*, 2014, **515**, 100–103.

15 M. Neumann, S. Füldner, B. König and K. Zeitler, Metal-Free, Cooperative Asymmetric Organophotoredox Catalysis with Visible Light, *Angew. Chem., Int. Ed.*, 2011, **50**, 951–954.

16 D. M. Schultz and T. P. Yoon, Solar Synthesis: Prospects in Visible Light Photocatalysis, *Science*, 2014, **343**, 1239176–1239176.

17 J.-H. Shon and T. S. Teets, Photocatalysis with Transition Metal Based Photosensitizers, *Comments Inorg. Chem.*, 2019, 1–33.

18 W. J. Finkenzeller and H. Yersin, Emission of Ir(ppy)3. Temperature dependence, decay dynamics, and magnetic field properties, *Chem. Phys. Lett.*, 2003, **377**, 299–305.

19 C. Kerzig, X. Guo and O. S. Wenger, Unexpected Hydrated Electron Source for Preparative Visible-Light Driven Photoredox Catalysis, *J. Am. Chem. Soc.*, 2019, **141**, 2122–2127.

20 S. Priya and J. D. Weaver, Prenyl Praxis: A Method for Direct Photocatalytic Defluoroprenylation, *J. Am. Chem. Soc.*, 2018, **140**, 16020–16025.

21 E. D. Nacsa and D. W. C. MacMillan, Spin-Center Shift-Enabled Direct Enantioselective α-Benzylation of Aldehydes with Alcohols, *J. Am. Chem. Soc.*, 2018, **140**, 3322–3330.

This journal is © the Partner Organisations 2021

Inorg. Chem. Front., 2021, **8**, 3253–3265 | **3263**

22 S. Senaweera and J. D. Weaver, Dual C–F, C–H Functionalization via Photocatalysis: Access to Multifluorinated Biaryls, *J. Am. Chem. Soc.*, 2016, **138**, 2520–2523.

23 M. S. Lowry, J. I. Goldsmith, J. D. Slinker, R. Rohl, R. A. Pascal, G. G. Malliaras and S. Bernhard, Single-Layer Electroluminescent Devices and Photoinduced Hydrogen Production from an Ionic Iridium(III) Complex, *Chem. Mater.*, 2005, **17**, 5712–5719.

24 J. I. Goldsmith, W. R. Hudson, M. S. Lowry, T. H. Anderson and S. Bernhard, Discovery and High-Throughput Screening of Heteroleptic Iridium Complexes for Photoinduced Hydrogen Production, *J. Am. Chem. Soc.*, 2005, **127**, 7502–7510.

25 W. Sattler, L. M. Henling, J. R. Winkler and H. B. Gray, Bespoke Photoreductants: Tungsten Arylisocyanides, *J. Am. Chem. Soc.*, 2015, **137**, 1198–1205.

26 L. A. Büldt, X. Guo, A. Prescimone and O. S. Wenger, A Molybdenum(0) Isocyanide Analogue of Ru(2,2′-Bipyridine)$_3$$^{2+}$: A Strong Reductant for Photoredox Catalysis, *Angew. Chem., Int. Ed.*, 2016, **55**, 11247–11250.

27 P. Herr, F. Glaser, L. A. Büldt, C. B. Larsen and O. S. Wenger, Long-Lived, Strongly Emissive, and Highly Reducing Excited States in Mo(0) Complexes with Chelating Isocyanides, *J. Am. Chem. Soc.*, 2019, **141**, 14394–14402.

28 T. U. Connell, C. L. Fraser, M. L. Czyz, Z. M. Smith, D. J. Hayne, E. H. Doeven, J. Agugiaro, D. J. D. Wilson, J. L. Adcock, A. D. Scully, D. E. Gómez, N. W. Barnett, A. Polyzos and P. S. Francis, The Tandem Photoredox Catalysis Mechanism of [Ir(ppy)$_2$(dtb-bpy)]$^+$ Enabling Access to Energy Demanding Organic Substrates, *J. Am. Chem. Soc.*, 2019, **141**, 17646–17658.

29 J.-H. Shon and T. S. Teets, Potent Bis-Cyclometalated Iridium Photoreductants with β-Diketiminate Ancillary Ligands, *Inorg. Chem.*, 2017, **56**, 15295–15303.

30 J.-H. Shon, S. Sittel and T. S. Teets, Synthesis and Characterization of Strong Cyclometalated Iridium Photoreductants for Application in Photocatalytic Aryl Bromide Hydrodebromination, *ACS Catal.*, 2019, **9**, 8646–8658.

31 J.-H. Shon, D. Kim, M. D. Rathnayake, S. Sittel, J. Weaver and T. S. Teets, Photoredox catalysis on unactivated substrates with strongly reducing iridium photosensitizers, *Chem. Sci.*, 2021, **12**, 4069–4078.

32 J.-H. Shon and T. S. Teets, Potent Bis-Cyclometalated Iridium Photoreductants with β-Diketiminate Ancillary Ligands, *Inorg. Chem.*, 2017, **56**, 15295–15303.

33 S.-C. Lo, C. P. Shipley, R. N. Bera, R. E. Harding, A. R. Cowley, P. L. Burn and I. D. W. Samuel, Blue Phosphorescence from Iridium(III) Complexes at Room Temperature, *Chem. Mater.*, 2006, **18**, 5119–5129.

34 T. Sajoto, P. I. Djurovich, A. Tamayo, M. Yousufuddin, R. Bau, M. E. Thompson, R. J. Holmes and S. R. Forrest, Blue and Near-UV Phosphorescence from Iridium Complexes with Cyclometalated Pyrazolyl or *N*

-Heterocyclic Carbene Ligands, *Inorg. Chem.*, 2005, **44**, 7992–8003.

35 Y. K. Radwan, A. Maity and T. S. Teets, Manipulating the Excited States of Cyclometalated Iridium Complexes with β-Ketoiminate and β-Diketiminate Ligands, *Inorg. Chem.*, 2015, **54**, 7122–7131.

36 R. M. Maya, A. Maity and T. S. Teets, Fluorination of Cyclometalated Iridium β-Ketoiminate and β-Diketiminate Complexes: Extreme Redox Tuning and Ligand-Centered Excited States, *Organometallics*, 2016, **35**, 2890–2899.

37 E. Kabir, Y. Wu, S. Sittel, B.-L. Nguyen and T. S. Teets, Improved deep-red phosphorescence in cyclometalated iridium complexes via ancillary ligand modification, *Inorg. Chem. Front.*, 2020, **7**, 1362–1373.

38 H. Na, L. M. Cañada, Z. Wen, J. I. Wu and T. S. Teets, Mixed-carbene cyclometalated iridium complexes with saturated blue luminescence, *Chem. Sci.*, 2019, **10**, 6254–6260.

39 L. M. Cañada, J. Kölling and T. S. Teets, Blue-phosphorescent bis-cyclometalated iridium complexes with aryl isocyanide ancillary ligands, *Polyhedron*, 2020, **178**, 114332.

40 H. Roth, N. Romero and D. Nicewicz, Experimental and Calculated Electrochemical Potentials of Common Organic Molecules for Applications to Single-Electron Redox Chemistry, *Synlett*, 2015, **27**, 714–723.

41 D. M. Arias-Rotondo and J. K. McCusker, The photophysics of photoredox catalysis: a roadmap for catalyst design, *Chem. Soc. Rev.*, 2016, **45**, 5803–5820.

42 J. W. Tucker, J. M. R. Narayanam, S. W. Krabbe and C. R. J. Stephenson, Electron Transfer Photoredox Catalysis: Intramolecular Radical Addition to Indoles and Pyrroles, *Org. Lett.*, 2010, **12**, 368–371.

43 B. Hu, Y. Li, W. Dong, K. Ren, X. Xie, J. Wan and Z. Zhang, Visible light-induced intramolecular dearomative cyclization of α-bromo-N-benzyl-alkylamides: efficient construction of 2-azaspiro[4.5]decanes, *Chem. Commun.*, 2016, **52**, 3709–3712.

44 W. Sattler, M. E. Ener, J. D. Blakemore, A. A. Rachford, P. J. LaBeaume, J. W. Thackeray, J. F. Cameron, J. R. Winkler and H. B. Gray, Generation of Powerful Tungsten Reductants by Visible Light Excitation, *J. Am. Chem. Soc.*, 2013, **135**, 10614–10617.

45 S. B. Harkins and J. C. Peters, A Highly Emissive Cu$_2$N$_2$ Diamond Core Complex Supported by a [PNP]$^-$ Ligand, *J. Am. Chem. Soc.*, 2005, **127**, 2030–2031.

46 J. M. Ahn, J. C. Peters and G. C. Fu, Design of a Photoredox Catalyst that Enables the Direct Synthesis of Carbamate-Protected Primary Amines via Photoinduced, Copper-Catalyzed *N*-Alkylation Reactions of Unactivated Secondary Halides, *J. Am. Chem. Soc.*, 2017, **139**, 18101–18106.

47 S. Baral-Tosh, S. K. Chattopadhyay and P. K. Das, A laser flash photolysis study of paraquat reduction by photogenerated aromatic ketyl radicals and carbonyl triplets, *J. Phys. Chem.*, 1984, **88**, 1404–1408.

3264 | *Inorg. Chem. Front.*, 2021, **8**, 3253–3265

This journal is © the Partner Organisations 2021

48 K. Kikuchi, C. Sato, M. Watabe, H. Ikeda, Y. Takahashi and T. Miyashi, New aspects of fluorescence quenching by molecular oxygen, *J. Am. Chem. Soc.*, 1993, **115**, 5180–5184.

49 J. N. Schrauben, M. Cattaneo, T. C. Day, A. L. Tenderholt and J. M. Mayer, Multiple-Site Concerted Proton–Electron Transfer Reactions of Hydrogen-Bonded Phenols Are Nonadiabatic and Well Described by Semiclassical Marcus Theory, *J. Am. Chem. Soc.*, 2012, **134**, 16635–16645.

50 M. J. Frisch, G. W. Trucks, H. B. Schlegel, G. E. Scuseria, M. A. Robb, J. R. Cheeseman, G. Scalmani, V. Barone, G. A. Petersson, H. Nakatsuji, X. Li, M. Caricato, A. V. Marenich, J. Bloino, B. G. Janesko, R. Gomperts, B. Mennucci, H. P. Hratchian, J. V. Ortiz, A. F. Izmaylov, J. L. Sonnenberg, D. Williams-Young, F. Ding, F. Lipparini, F. Egidi, J. Goings, B. Peng, A. Petrone, T. Henderson, D. Ranasinghe, V. G. Zakrzewski, J. Gao, N. Rega, G. Zheng, W. Liang, M. Hada, M. Ehara, K. Toyota, R. Fukuda, J. Hasegawa, M. Ishida, T. Nakajima, Y. Honda, O. Kitao, H. Nakai, T. Vreven, K. Throssell, J. A. Montgomery Jr., J. E. Peralta, F. Ogliaro, M. J. Bearpark, J. J. Heyd, E. N. Brothers, K. N. Kudin, V. N. Staroverov, T. A. Keith, R. Kobayashi, J. Normand, K. Raghavachari, A. P. Rendell, J. C. Burant, S. S. Iyengar, J. Tomasi, M. Cossi, J. M. Millam, M. Klene, C. Adamo, R. Cammi, J. W. Ochterski, R. L. Martin, K. Morokuma, O. Farkas, J. B. Foresman and D. J. Fox, *Gaussian 16 Rev. C.01*, Wallingford, CT, 2016.

51 J. P. Perdew, K. Burke and M. Ernzerhof, Generalized Gradient Approximation Made Simple, *Phys. Rev. Lett.*, 1996, **77**, 3865–3868.

52 M. Dolg, U. Wedig, H. Stoll and H. Preuss, Energy–adjusted ab initio pseudopotentials for the first row transition elements, *J. Chem. Phys.*, 1987, **86**, 866–872.

53 E. Cancès, B. Mennucci and J. Tomasi, A new integral equation formalism for the polarizable continuum model: Theoretical background and applications to isotropic and anisotropic dielectrics, *J. Chem. Phys.*, 1997, **107**, 3032–3041.

54 B. Mennucci, E. Cancès and J. Tomasi, Evaluation of Solvent Effects in Isotropic and Anisotropic Dielectrics and in Ionic Solutions with a Unified Integral Equation Method: Theoretical Bases, Computational Implementation, and Numerical Applications, *J. Phys. Chem. B*, 1997, **101**, 10506–10517.

55 S. Miertuš, E. Scrocco and J. Tomasi, Electrostatic interaction of a solute with a continuum. A direct utilizaion of AB initio molecular potentials for the prevision of solvent effects, *Chem. Phys.*, 1981, **55**, 117–129.

56 S. I. Gorelsky and A. B. P. Lever, Electronic structure and spectra of ruthenium diimine complexes by density functional theory and INDO/S. Comparison of the two methods, *J. Organomet. Chem.*, 2001, **635**, 187–196.

57 S. I. Gorelsky, *AOMix: Program for Molecular Orbital Analysis*, York University, Toronto, 1997, http://www.sg-chem.net. Accessed January 2018.

58 G. M. Sheldrick, A short history of *SHELX*, *Acta Crystallogr., Sect. A: Found. Crystallogr.*, 2008, **64**, 112–122.

59 A. L. Spek, Structure validation in chemical crystallography, *Acta Crystallogr., Sect. D: Biol. Crystallogr.*, 2009, **65**, 148–155.

This journal is © the Partner Organisations 2021

Inorg. Chem. Front., 2021, **8**, 3253–3265 | **3265**